MASARYKOVA UNIVERZITA
PŘÍRODOVĚDECKÁ FAKULTA
ÚSTAV TEORETICKÉ FYZIKY A ASTROFYZIKY

Bakalářská práce

BRNO 2021 KLAUDIA PROTUŠOVÁ

MASARYKOVA UNIVERZITA
Přírodovědecká fakulta
Ústav teoretické fyziky a astrofyziky

Rentgenová studie sférického šoku v galaxii M89 vyvolaného působením aktivního galaktického jádra

Bakalářská práce

Klaudia Protušová

Vedoucí práce: doc. Mgr. Norbert Werner, Ph.D. Brno 2021

Bibliografický záznam

Autor:	Klaudia Protušová Přírodovědecká fakulta, Masarykova univerzita Ústav teoretické fyziky a astrofyziky
Název práce:	Rentgenová studie sférického šoku v galaxii M89 vyvolaného působením aktivního galaktického jádra
Studijní program:	Fyzika
Studijní obor:	Astrofyzika
Vedoucí práce:	doc. Mgr. Norbert Werner, Ph.D.
Akademický rok:	2020/2021
Počet stran:	viii + 35
Klíčová slova:	Galaxie: Shluky: Obecné; Galaxie: Individuální: NGC číslo: NGC 4552; Galaxie: Individuální: Messier číslo: M89; Galaxie: Mezigalaktická hmota; Galaxie: Mezigalaktická hmota: Jaderné výrony; Šokové vlny; Rentgenová studie: Galaxie; Astrofyzika: Vysoko energetická astrofyzika

Bibliographic Entry

Author:	Klaudia Protušová Faculty of Science, Masaryk University Department of theoretical physics and astrophysics
Title of Thesis:	X-ray study of the AGN driven spherical shock in the giant elliptical galaxy M89
Degree Programme:	Physics
Field of Study:	Astrophysics
Supervisor:	doc. Mgr. Norbert Werner, Ph.D.
Academic Year:	2020/2021
Number of Pages:	viii + 35
Keywords:	Galaxies: Clusters: General; Galaxies: Individual: NGC Number: NGC 4552; Galaxies: Individual: Messier Number: M89; Galaxies: Intergalactic Medium; Galaxies: Intergalactic Medium: Nuclear Outflows; Shock waves; X-Rays: Galaxies; Astrophysics: High Energy Astrophysics

Abstrakt

Představujeme výsledky z 200 ks *Chandra* pozorování působení jaderného výronu v eliptické galaxii NGC 4552 (M89). *Chandra* snímek této galaxie v energetickém rozhraní 0.5-2.0 keV odhaluje dvě prstencové struktury přibližně $\sim$1.3 kpc daleko od středu galaxie, což bylo zjištěno v dřívější studii od Machacek, Jones, Forman & Nulsen (2006). V naší hlubší studii používáme spektrální analýzu a jednoduchý sféricky symetrický bodový model šoku povrchové jasnosti, díky čemuž argumentujeme, že tyto šoky jsou konzistentní s Mach 1.6 šokovým modelem.

Abstract

We present results from a deep (200 ks) *Chandra* observation of the nuclear outflow activity found in the elliptical galaxy NGC 4552 (M89). *Chandra* images in the 0.5-2.0 keV band show two ring-like structures approximately $\sim$1.3 kpc away from the centre of the galaxy, as was formerly reported by Machacek, Jones, Forman & Nulsen (2006). In our deeper study, we use spectral analysis and a simple spherically symmetric point explosion shock model across the surface brightness profile to argue that these shocks are consistent with a Mach 1.6 shock model.

MUNI
SCI

MASARYKOVA UNIVERZITA
PŘÍRODOVĚDECKÁ FAKULTA
KOTLÁŘSKÁ 2, 611 37 BRNO
IČ: 00216224
DIČ: CZ00216224

ZADÁNÍ BAKALÁŘSKÉ PRÁCE

Akademický rok: 2020/2021

Ústav:	Přírodovědecká fakulta
Studentka:	Klaudia Protušová
Program:	Fyzika
Obor:	Astrofyzika

Ředitel *ústavu* PřF MU Vám ve smyslu Studijního a zkušebního řádu MU určuje bakalářskou práci s názvem:

Název práce:	Rentgenová studie sférického šoku v galaxii M89 vyvolaného působením aktivního galaktického jádra
Název práce anglicky:	X-ray study of the AGN driven spherical shock in the giant elliptical galaxy M89
Jazyk závěrečné práce:	angličtina

Oficiální zadání:
Observations of nearby galaxies with the Chandra X-ray observatory allow us to study directly the interaction of central accreting supermassive black holes with the hot gaseous atmospheres permeating the galaxies. The X-ray images typically reveal cavities, which are buoyant bubbles inflated by the jet emanating from the central active galactic nucleus (AGN). In some relatively rare cases the X-ray observations also show the presence of weak spherical shocks propagating away from the central AGN. One of the most prominent shocks is observed in the galaxy NGC 4552 (M89), which resides in the Virgo cluster of galaxies. The student will analyse relatively recent deep Chandra X-ray data of this galaxy in order to determine the properties of the shock, such as its Mach number and the corresponding mechanical power produced by the central AGN, as well other AGN feedback related features.

Vedoucí práce:	doc. Mgr. Norbert Werner, Ph.D.
Datum zadání práce:	11. 11. 2020
V Brně dne:	26. 5. 2021

Zadání bylo schváleno prostřednictvím IS MU.

Klaudia Protušová, 21. 1. 2021
doc. Mgr. Norbert Werner, Ph.D., 26. 1. 2021
Mgr. Michael Krbek, Ph.D., 1. 2. 2021

Poďakovanie

Na tomto mieste by som chcela poďakovať v prvom rade svojmu vedúcemu Norbertovi Wernerovi za trpezlivosť a každú radu k výskumu. Ďalej by som chcela poďakovať Jean-Paul Breuerovi a Tomášovi Plškovi za pomoc a odpovede ku každej otázke pri spracovávaní dát.

Prehlásenie

Prehlasujem, že som svoju bakalársku prácu vypracovala samostatne pod vedením svojho vedúceho práce s využitím informačných zdrojov, ktoré sú v práci citované.

Brno 4. júna 2021 ....

Klaudia Protušová

Contents

Acronyms

Presented are all acronyms used in this text in the order of their appearance.

AGN	Active galactic nuclei
ICM	Intracluster medium
LINER	Low-ionization nuclear emission-line region
CXO	Chandra X-ray Observatory
NASA	National Aeronautics and Space Administration
HRMA	High Resolution Mirror Assembly
FOV	Field of view
ACIS	Advanced CCD Imaging Spectrometer
HRC	High Resolution Camera
CCD	Charge-coupled device
LETGS	Low Energy Transmission Grating Spectrometer
HETGS	High Energy Transmission Grating Spectrometer
SAO	Smithsonian Astrophysical Observatory
ObsID	Observation Id
CIAO	Chandra Interactive Analysis of Observations
CTI	Charge transfer inefficiency
VFAINT	Very faint
WCS	World Coordinate System
PSF	Point spread function

Introduction

During the 20th century, many sciences underwent a revolution with new techniques and instruments, with astronomy and astrophysics being no exception to that. With the new technology, scientists were able to observe the Universe with the entirety of the electromagnetic spectrum. These new observation techniques led to a discovery of many new phenomena, with one of them being an active galactic nucleus. An active galactic nucleus, often abbreviated to AGN, is a compact region in the centre of galaxies with a much higher-than-normal luminosity with characteristics that suggest this radiation is not emitted by stars. The AGNs, however, shape the morphology of the intracluster medium around, resulting in various structures, such as X-ray cavities, shock fronts, or jets in radio emission. One such galaxy showcasing these features in X-rays is the elliptical galaxy NGC 4552 or M89 with two distinct ring-like structures indicating a recent outburst of its AGN, and a stripped tail caused by the galaxy's movement through the ambient medium.

In 2006, a thorough examination of these distinct structures in this galaxy were described by Machacek, Jones, Forman & Nulsen (2006) and Machacek, Nulsen, Jones & Forman (2006), with 54.4 ks of available *Chandra* data. These studies included an imaging analysis used to determine the radius of the the shock along with determination of the extend of the tail extending from the galaxy. Moreover, both studies used spectral analysis to determine the temperature and abundances of these features, while a surface brightness profiling was used on the shock rings only to determine the speed, mechanical power, and age of the recent outburst. Since then, the number of data has quadrupled which led Kraft et al. (2017) to re-examine the research done about the tail trailing behind the galaxy in 2017. The deeper study has revealed before unseen parts and helped better map the morphology of these structures. However, Kraft et al. (2017) did not re-examine the shock rim caused by a recent AGN activity. Seeing as this research with deeper data proved to update previous conclusions, we have decided to review the study of the ring-like features to complete the re-examination of NGC 4552 with bigger dataset, and determine whether the conclusions drawn previously were correct.

This thesis is organised as follows. In chapter 1 we delve into the theory behind the intracluster medium and its importance regarding various structures which may be observed within. In chapter 2 we identify AGNs and their influence upon the ICM while also explaining the physics behind shocks which appear due to AGN activity. With the theoretical part completed, we introduce the object of our study NGC 4552 in chapter 3, describe its properties and structures observed in X-rays determined by previous research, specifically the stripped tail and shock rings. Afterwards we present the data and summary of the data preparation in chapter 4. Our data processing encapsulates the background subtracted, exposure-corrected image in the energy band of 0.5-2.0 keV which shows the distinct shock rings at $r \sim 1.3$ kpc from the centre of the galaxy, modelling of the spectral properties across the rim, and last but not least the surface brightness estimating the density jump at the edge of the shock. In this chapter we also provide the discussion of our analysis and comparison to previous studies. At last, we end our thesis with a brief summary of our results and the entire work.

Chapter 1

Hot atmospheres

The largest gravitationally-bound structures in the universe are galaxy clusters with diameters of several megaparsecs and masses up to $10^{15}\ M_{\odot}$, whose composition primarily consists of dark matter, and which takes up about 80 per cent of the total mass of the cluster. Dark matter, however, cannot be detected yet in any other way than by its gravitational effect on surrounding matter and light passing close by. The other 20 per cent of galaxy clusters is found in the form of baryonic matter, where only a fraction creates objects such as stars, planets, asteroids, and others.

The larger fraction of the visible matter is in the form of a hot, dilute, X-ray emitting plasma, which fills the space between galaxies. This plasma is often referred to with many terms, depending on the scale of the radii, e.g. *the interstellar medium (ISM)* when observed at interstellar distances, at larger radii it is *the circumgalactic medium (CGM)*, in galaxy groups it is known as *the intragroup medium (IGrM)*, in galaxy clusters as intracluster medium (ICM), and in the cosmic web filaments as *the intergalactic medium (IGM)* or *warmhot intergalactic medium (WHIM)*. In our research we move within the range of galaxies and will simply refer to all these stages of ambient medium as either ICM, hot atmospheres, or hot gas to stay consistent with the literature regarding this subject.

The ICM forms a hydrostatic atmosphere permeating clusters, where the gravitating mass is represented by the temperature and density distributions. The density of the hot X-ray emitting atmospheres ranges from approximately 10^{-1} cm^{-3} in the centre of the cluster to 10^{-4} cm^{-3} towards the outskirts. For most clusters, the temperature of hot atmospheres reaches 10^7–10^8 K, where the temperature is depended on the mass of the cluster as described in Bykov et al. (2015). These extreme temperatures lead to strong ionization of the gas, thus the ICM consists of fully ionized hydrogen and helium, and is additionally enriched with heavier elements. The metallicity of hot atmospheres ranges from about a third of the metallicity of the Sun increasing to around Solar at the centres (Werner & Mernier 2020).

The examination of hot atmospheres present in these giant structures can be done using X-ray space observatories. The first observatory to detect them as X-ray sources was the

Uhuru satellite launched in 1970, while today the observations are mainly done using *XMM-Newton*, and *Chandra X-ray Observatory*, which will be described in detail in section 4.1.

1.1 X-ray emission

At the densities and temperatures of hot atmospheres, the ICM can generally be treated as an optically thin coronal plasma in ionization equilibrium, which emits radiation via interactions between particles, precisely free electrons and nuclei it consists of. These interactions can be divided into three categories; the de-excitation (bound-bound), recombination (free-bound), and bremsstrahlung (free-free).

The bremsstrahlung emission process, operating on the basis of deceleration of an electron deflected by atomic nucleus, emits a photon that can be detected in the X-ray wavelengths. The emissivity ε of these bremsstrahlung photons is scaled as

$$\varepsilon = \bar{g} n_{\mathrm{e}}^2 (kT_{\mathrm{e}})^{-1/2} e^{-E/kT_{\mathrm{e}}} \,, \tag{1.1}$$

where $\bar{g}$ is the Gaunt-factor, a quantum mechanical correction factor weakly depending on the photon energy, k is the Boltzmann constant, T_{e} is the electron temperature, and n_{e} is the electron density of hot atmospheres. The electron in this process remains free after the emission of a photon, and the subsequent radiation has a continuous profile, seeing as there are no restrictions of the energy quantum emitted by this process.

The other two processes rely on a free electron and a nucleus forming a bound system, and are a trace of the highly ionized heavier elements present in hot gas. In the free-bound process, also known as radiative recombination, an electron moves too close to a nucleus, which consequently captures it, resulting in their recombination. The electron can be captured to the ground state, and the emitted photon has energy greater than the ionization energy, which results in a continuous spectrum.

Alternatively, in the free-bound process, the electron recombines to an excited state with the emission of a photon with energy lower than the ionization energy, after which the electron cascades down through the excited states to the ground state. The de-excitation process happens in a bound electron - nucleus system, where an electron falls from an excited energy level to the ground state. These transitions result in discrete spectral lines, each corresponding to a specific ion of a specific element.

Because there is no uniform way for these photons to be emitted, and can happen from any of the three above mentioned interactions, they all contribute to the X-ray spectrum. However, the thermal bremsstrahlung emission dominates among the spectrum in rich, massive clusters permeated by gas with temperatures higher than $10^{7.5}$ K (or kT $\gtrsim$ 3 keV). In cooler gas pervading groups and elliptical galaxies with temperatures in the range $10^{6.5}$-$10^{7.5}$ K (kT $\sim$ 0.3 - 3 keV), the plasma is less ionized, which means that the emission

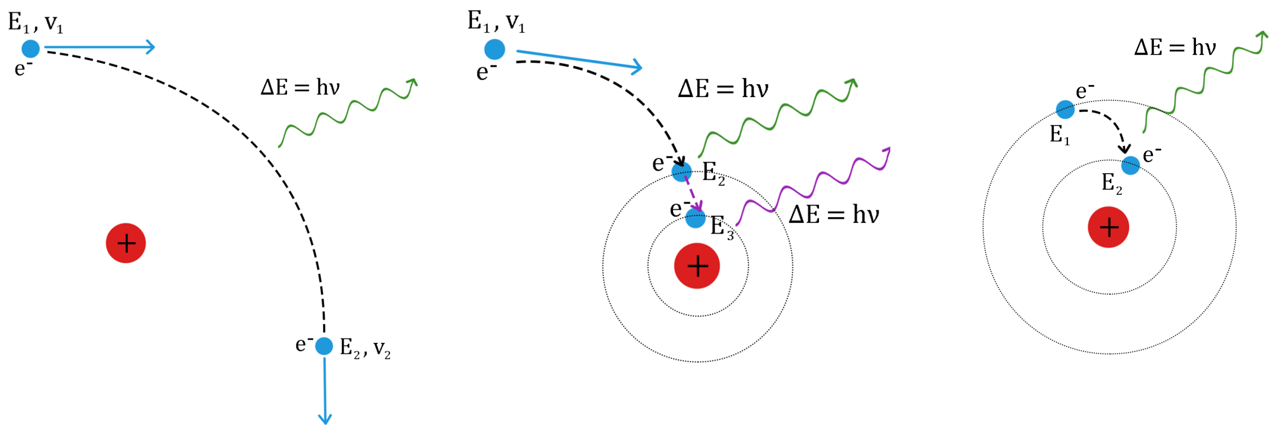

Figure 1.1: Graphic representation of (*left*) bremsstrahlung emission, (*middle*) radiative recombination, and (*right*) the de-excitation process.

lines corresponding to atomic transitions are more prevalent than, and can even dominate over, bremsstrahlung emission (see Werner & Mernier 2020).

1.1.1 Spectroscopy

Examining the spectra of hot atmospheres can help us look further into the properties of the intracluster medium, which can be typically achieved by fitting the data with spectral models of plasma emission with several free parameters.

The most important qualities which can be derived from spectral fitting are the electron density of hot gas, which is directly proportional to the square root of X-ray luminosity. To calculate this value, we first need to determine the emission measure $Y = \int n_\mathrm{e} n_\mathrm{H} dV$ from spectral fitting, where n_H is the number density of protons while V is the volume of the emitting source. After estimating a reasonable volume of the source and applying smooth gas distribution within this area, the gas density value can be determined easily.

Another important parameter of the ICM which can be found in the spectra is its temperature, which can be determined via the shape of the observed continuum. When dealing with spectra dominated with spectral lines from cooler sources, the relative intensities of these lines provide an additional constraint on the temperature of the gas. Additionally, when examining the emission lines of ions of particular elements, the abundance of each respective element can be derived. This can be achieved by measuring the equivalent width of each emission line which is equal to the ratio between flux of the line compared to the flux of the continuum at corresponding position.

After acquiring these parameters, we are able to determine the pressure and entropy of the gas as well. Because of the low density of the ICM and its almost exact nature of ideal gas, we can simply express pressure by

$$P = \frac{\rho nkT}{\mu m_{\mathrm{p}}} = nkT \propto n_{\mathrm{e}} , \tag{1.2}$$

where ρ is the gas density, m_{p} is the mass of a proton, and $\mu \simeq 0.6$ is the mean molecular mass in units of proton mass.

In astrophysics, however, entropy is actually the adiabatic constant, and does not equal to thermodynamic entropy. The gas entropy of the ICM can be expressed by

$$K = \frac{kT}{n_e^{2/3}} . \tag{1.3}$$

This entropy relates to the thermodynamic entropy as

$$\Delta S = 3/2 \ln K . \tag{1.4}$$

This property serves as a documentation of the thermodynamic history of the ICM because it can only be changed by shocks, radiative cooling, conduction, or mixing of the gas (Werner & Mernier 2020).

1.2 Fall of galaxies through the ICM

The ICM, while very tenuous, can still be deeply affected by the activity of its inhabitants. One of the ways that galaxies alter it is by their movement through the ICM. Their infall can leave a variety of visible imprints in the gas, such as stretched tails of galaxy gas found to extend 10 to 200 kpc before fading into the ambient gas. However, this movement causes a change in the corona of the infalling object as well. As a result of its motion, the infalling galaxy experiences a head wind that places ram pressure on the galaxy's hot atmosphere, causing it to be stripped away.

Nonetheless, ram pressure stripping may not appear in every single galaxy that is moving through hot atmospheres. It occurs only in the cases where the wind is strong enough to overcome the restoring gravitational force of the galaxy to remove the gas contained within it. This pressure can strip gas out of the galaxy where, essentially, the gas is gravitationally bound to the galaxy less strongly than the force from the intracluster medium 'wind' due to the ram pressure as described in Gunn & Gott (1972). The ram pressure experienced by the galaxy moving through the ICM would be:

$$P_r \approx \rho_{\mathrm{e}} v^2 , \tag{1.5}$$

where P_r is the ram pressure, ρ_{e} is the density of the ICM gas and v is the speed of the galaxy relative to the medium.

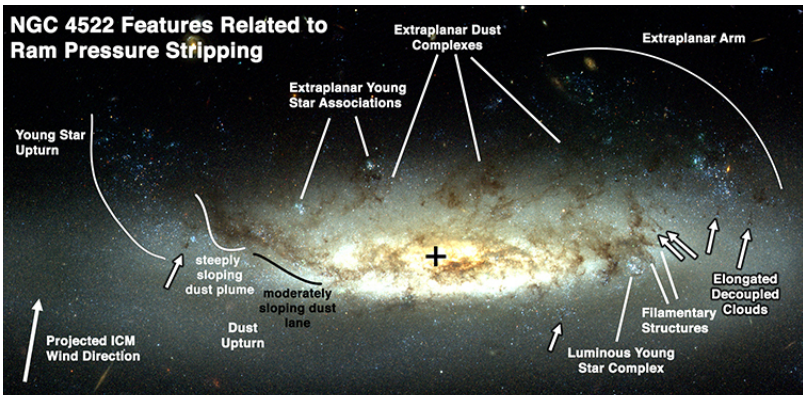

Figure 1.2: An example of ram-pressure stripping of a lower mass cold-gas rich star forming galaxy NGC 4522. Image credit: Abramson et al. (2016).

1.3 Fluid mechanics of the ICM

Despite their very low density, the motion of hot atmospheres surrounding the galaxies inside clusters can be described by fluid mechanics. As the galaxies move through the ICM, they create tails, and cold fronts of gas with higher density as described above, while the AGN activity adds even more discrepancies in the distribution of the gas (which will be described in chapter 2). All of the changes created by galactic activity in the density and temperature of hot gas are counterbalanced according to the laws of fluid mechanics. If every activity altering the distribution of matter in the atmosphere was removed, it would reach hydrostatic equilibrium with the underlying gravitational potential Φ, balancing the gravitational force by the pressure gradient of the gas, described by:

$$\frac{1}{\rho}\frac{\mathrm{d}P}{\mathrm{d}t} = -\frac{\mathrm{d}\Phi}{\mathrm{d}r} = -\frac{GM_{\mathrm{tot}}}{r^2}\,, \tag{1.6}$$

where G is the gravitational constant and M_{tot} is the total mass of the system, encompassing the dark matter, stars, and gas. From the assumption of hydrostatic equilibrium we are able to derive the total mass distribution of the system by measuring basic properties of its X-ray emitting gas. The total mass distribution can be calculated from:

$$M_{\mathrm{tot}}(<r) = -\frac{kT(r)r}{G\mu m_p}\left(\frac{\mathrm{d}\ln T}{\mathrm{d}\ln r} + \frac{\mathrm{d}\ln\rho}{\mathrm{d}\ln r}\right)\,. \tag{1.7}$$

All that is needed to obtain an accurate result of the total mass within a certain radius is for the data to be good enough to derive the spatial distribution of the gas density and temperature, as stated in Werner & Mernier (2020).

Chapter 2

Active galactic nuclei

In comparison to average galaxies, active galaxies have a small core of emission embedded at their center, with the core being usually highly variable and bright compared to the rest of the galaxy. The research behind what hides in the center of these bright galactic nuclei is still ongoing, with the X-ray emission of these objects providing many clues about what is hiding behind the dust clouds. Observations of AGN in X-ray showed a simple source that could change variability over a short period of time, indicating that the source has a fairly small area. Combined with the rapid high energy output, it is now well established that the most likely candidate for the driving force behind these AGNs are supermassive black holes.

2.1 AGN feedback

Massive elliptical galaxies at the centres of clusters host supermassive black holes with masses higher than $10^9\ M_\odot$. These black holes, when accreting matter, are one of the most effective engines in the entire universe, when converting accreting matter into energy. Black holes of this scale should be releasing about 10^{47} erg s^{-1} when accreting matter, and converting this matter to energy yields about 10^{20} ergs per gram of accreted material (Fabian 2012).

This energy can be released in two different forms; either in a radiative or mechanical form, depending on the rate of accretion and the structure of the accretion flow. The tremendous amount of energy released in those two forms were quickly realized to be fundamental forces that could influence the evolution of galaxies. In the radiative AGN feedback, also called the ”quasar mode”, the radiation pressure caused by the black hole accreting matter combines with the cold gas. This pressure drives high velocity, high mass outflows that have the potential to remove or destroy the molecular gas found in its host galaxy (Fabian 2012). With effective mechanical coupling, characterized by jets of charged particles, they could heat the gas in and around galaxies isotropically. This constant heating of gas, sometimes referred to as ”maintenance mode”, has gathered convincing evidence due to X-ray observations of cavities created by radio jets, and lobes with displaced gas caused by its activity(McNamara & Nulsen 2012).

Needless to say, it is believed that all AGNs were at some point in their radiative mode, some even switching modes during the epochs. However, it is still unclear what caused these AGNs to turn from one mode to the other. Furthermore, there is little consensus on how the feedback loop is created and maintained. For the cool or cooling gas to fuel the AGN, the thermal state of the AGN would dictate the energy output of the supermassive black hole. One of the attempts to solve this problem which garnered support is the theory of ”precipitation” (Gaspari et al. (2013), Voit et al. (2015), McNamara et al. (2016)). The theory assumes that the gas condenses into cooler clouds which then fall towards the center, the same way as water vapour condenses and later falls in our own atmosphere. This would increase the accretion rate of the AGN and trigger a feedback loop (Werner & Mernier 2020).

2.2 AGN effect on star formation

Based on the classification shown above, we can sort the observed AGNs into two categories: those, whose energetic output is mostly radiative (radiative AGN) and those where mechanical energy output dominates over the other. While the radiative AGNs are predominantly bright in X-rays, the mechanically-dominated AGNs are usually found via radio observations. Both are also found in galaxies with vastly different stellar population; with the mechanically-radiative being dominant in galaxies with little to no new stars, whereas the radiative AGNs reside in galaxies with an on-going star formation. This has let many astrophysicists to drawing the conclusion that star formation and the accretion mechanisms of supermassive black holes are linked.

These conclusions have led to an increase in the number of studies investigating star formation rates of galaxies hosting AGNs. For the purely mechanically-dominated AGNs, we have found that they consistently reside in galaxies with low star-formation rate. These galaxies are observed as having massive lobe-like structures in the X-ray emission, inflated by the expanding AGN jets, and filled with radio emitting plasma. The lobes consequently displace the hot gas found inside the galaxy, creating cavities and driving weak shocks in the X-ray emitting plasma. These shocks thereafter heat the surrounding gas, preventing its cooling which is fundamental for star-formation. Therefore, no new stars are born (Werner & Mernier 2020).

However, for radiative AGNs, the results are not so uniform, and vary widely, with some studies claiming that AGN activity has no impact on star-formation, some claiming it enhances it, while others say that it’s actually hindering it. Moreover, some studies have actually shown that star-formation was either inhibited or boosted in the same galaxy, depending on the wave-band used to trace the AGN luminosity. Studies indicating these results are talked about in Harrison (2017). These contradicting conclusions can be largely

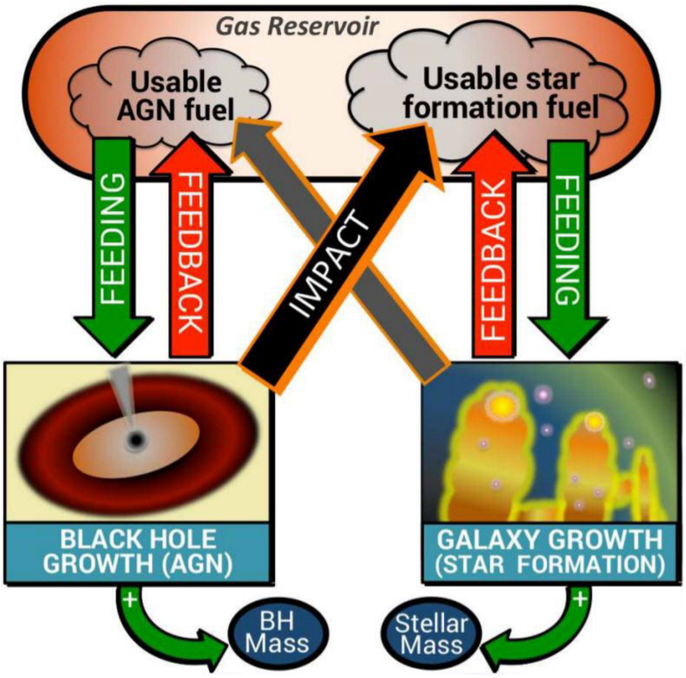

Figure 2.1: A schematic diagram showcasing the relationships between fuel supply, galaxy growth and black hole growth. Taken from Harrison (2017)

attributed to each research group using different samples and approaches. The biggest factor for these variations in results is the selection bias – for example, some studies take into account only radio bright samples which may contain not only the radiative AGN but also the mechanically dominated ones. Other factors may be the low number of the most luminous AGNs, difficulty with the conversion of photometric data to star-formation rates, etc. (Harrison 2017).

2.3 Nuclear outflows and shocks

As mentioned in the previous section, the mechanically dominant AGNs displace plasma away from the core via outbursts, which is supported by observations of X-ray dim regions defined by bright X-ray shells. The shocks created by the outbursts of a supermassive black hole create a discrepancy in the gas density, which is also accompanied by a drop in temperature. These fronts of displaced gas are identified by a sharp jump in the surface brightness of the object, which is a direct result of gas and temperature changes.

These shocks are, in spite of what we might expect, collision-less because of the low density of the gas, and therefore do not follow the same rules as shocks in e.g. the Earth's atmosphere. Shocks in astrophysical plasma are described by Rankine–Hugoniot conditions which describe the relations between the states on both sides of a shock wave. In a coordinate system that is connected to the discontinuity, the Rankine–Hugoniot conditions can be expressed as

$$\rho_1 v_1 = \rho_2 v_2 \equiv m \quad \text{Conservation of mass} \tag{2.1}$$
$$\rho_1 v_1^2 + P_1 = \rho_2 v_2^2 + P_2 \quad \text{Conservation of momentum} \tag{2.2}$$
$$h_1 + \frac{1}{2} v_1^2 = h_2 + \frac{1}{2} v_2^2 \quad \text{Conservation of energy,} \tag{2.3}$$
$$\tag{2.4}$$

where m is the mass flow rate per unit area, ρ_1, v_1, P_1 and h_1 are the mass density, fluid velocity, pressure, and enthalpy respectively describing the upstream area of the wave, while ρ_2, v_2, P_2 and h_2 describe the downstream area (Williams 2018). From the conservation of momentum we can derive the shock compression ratio as

$$\chi \equiv \frac{\rho_2}{\rho_1} = \frac{v_2}{v_1} \, . \tag{2.5}$$

For strong shocks we neglect the upstream pressure, which gives us the equation:

$$\chi = \frac{(\gamma + 1) M_1^2}{(\gamma - 1) M_1^2 + 2} \, , \tag{2.6}$$

where γ is the adiabatic index and M_1 is the Mach number. For non-relativistic gas we have $\gamma = 5/3$ which gives us shock ratio $\chi = 4$, and $M_1^2 \to \infty$. However, χ does not reach this value in our case, as we are dealing with weak shocks. Shocks propagating from one side of the gas to another can accelerate particles by having them cross the shock front multiple times as shown in Figure 2.2. This acceleration of particles is also known as diffusive shock theory. The compression ratio can also be expressed as a ratio between the densities found at the rim of the shock. Therefore, we can write the previous equation as

$$\chi = \frac{n_{\text{rim}}}{n_{\text{out}}} = \frac{(\gamma + 1) M_1^2}{(\gamma - 1) M_1^2 + 2} \, , \tag{2.7}$$

which predicts discontinuities in temperature as:

$$\frac{T_{\text{rim}}}{T_{\text{out}}} = \frac{(2\gamma M_1^2 - (\gamma - 1))((\gamma - 1) M_1^2 + 2)}{(\gamma + 1)^2 M_1^2} \, , \tag{2.8}$$

as presented in Machacek, Jones, Forman & Nulsen (2006). Therefore, we can estimate the Mach number of a shock by measuring the temperature and density ratio inside and outside the shock edge.

The Mach number of the shock front can be calculated using the temperatures measured by spectral fitting of the shocked and unshocked gas in front of the shock front. To estimate the shock speed via the density discontinuity, a model was proposed which assumes that the gas and the galaxies are in equilibrium in the same potential, while taking the isothermal and adiabatic equations for the state of the gas into account (Cavaliere & Fusco-Femiano 1976). For the simplest case, where the shock front is circular, we can assume that the model can be described by a symmetric broken power law distribution for the electron density as a function of radius expressed as

$$n_e = \begin{cases} n_{\rm rim} \left(\frac{r}{r_{\rm rim}} \right)^{-\alpha_1} & r < r_{\rm rim} \\ \frac{n_{\rm rim}}{\chi} \left(\frac{r}{r_{\rm rim}} \right)^{-\alpha_2} & r \geq r_{\rm rim} \; , \end{cases}$$

where $r_{\rm rim}$ is the outer radius or rim of the shock ring, $n_{\rm rim}$ and α is the normalization and power law index respectively for each region, and χ is the compression ratio (also called the "jump" parameter), from which the speed of shock or Mach number M_1 can be derived (Zhang et al. 2018), as discussed above. The "jump" parameter can be estimated via surface brightness profile fit over the edge of the density discrepancy, which will be described in more detail in subsection 4.2.3.

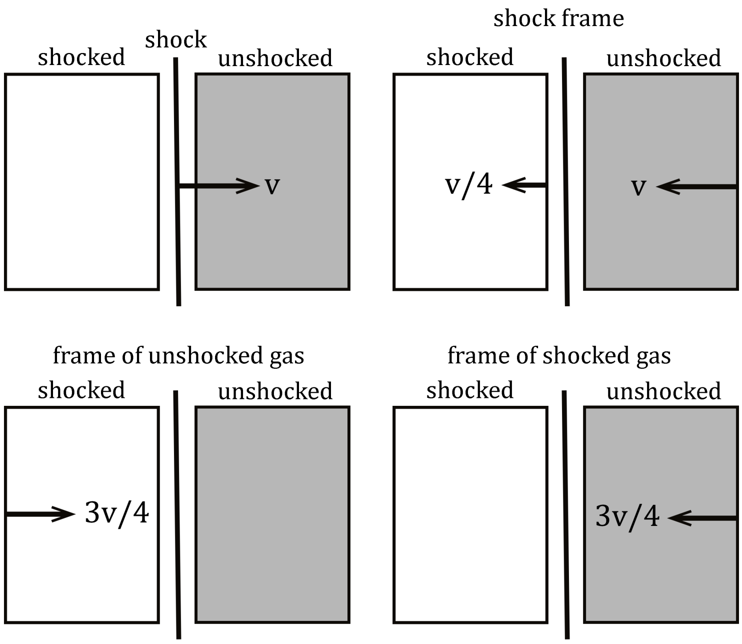

Figure 2.2: Schematics of different frames of the shock front where v denotes the velocity of the subject. When particle crosses across the cold front, it can gain energy from the shocked material by crossing the threshold multiple times. Based on (Rosswog & Bruggen 2007).

Chapter 3

M89

M89 (also known as NGC 4552) is an elliptical galaxy in the Virgo constellation with equatorial coordinates of $\alpha = 12^{\mathrm{h}}\ 35^{\mathrm{m}}\ 39.8^{\mathrm{s}}$ and $\delta = 12^{\circ}\ 33'\ 23''$ with the apparent magnitude of 9.8 mag, situated in the subcluster A of the Virgo cluster. A dominant representative of this subcluster is M87, which is located $72'$ in the eastern direction from M89. We assume that the distance from NGC 4552 to the Milky Way galaxy is 17 Mpc, which is consistent with the surface brightness fluctuation measurement of the distance to subcluster A (Frommert & Kronberg 2007, Kraft et al. 2017).

Discovered in 1781 along other 7 galaxies in the cluster by Charles Messier, M89 contains approximately 100 billion stars and more than 2000 globular star clusters. The galaxy is, according to the latest observations, nearly spherical with its apparent dimensions being $5.1 \times 4.7'$. The spherical nature of NGC 4552 could, however, be a trick of perspective, and be caused by its orientation relative to the Earth, with the ellipsoid appearing circular.

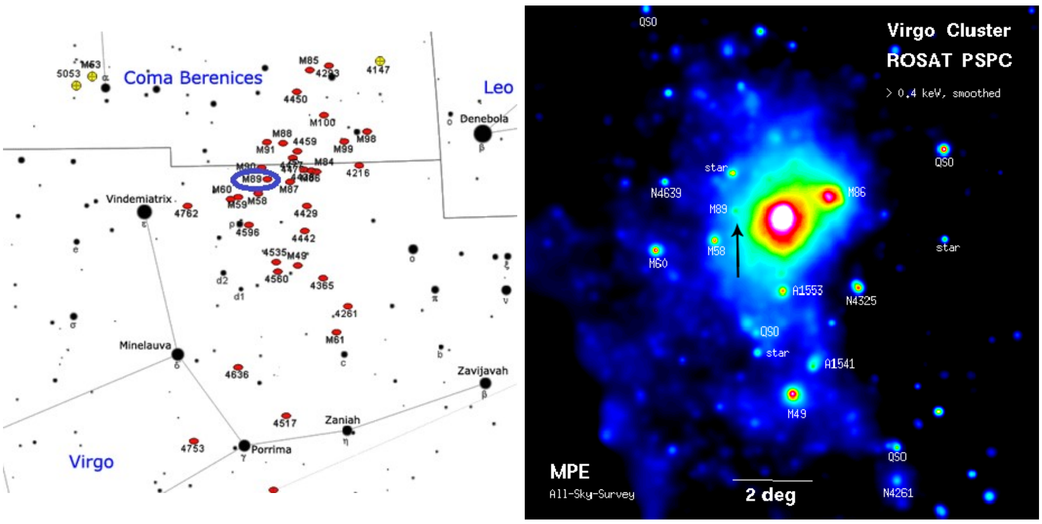

Figure 3.1: (*left*) Position of M89 in the night sky. (*right*) Position of M89 denoted by an arrow within the Virgo Cluster (Böhringer et al. 1994).

The galaxy moreover features a peculiar faint enveloping structure of gas and dust, extending up to ∼50 kpc from the galaxy, and a jet-like structure extruding through the galaxy up to ∼35 kpc, which was discovered by photographic amplification technique applied by David Malin. After a deeper study of M89 and its outer halo in the visible band, a system of complex shells has been discovered. This system indicates that the galaxy has underwent either multiple accretions, numerous merger events with satellite galaxies, or a single major merger event (Malin 1979, Clark et al. 1987, Janowiecki et al. 2010).

3.1 Ram-pressure in M89

As mentioned in section 1.3, galaxies falling through the ICM need to move supersonically for ram-pressure stripping to occur. When the distance modulus of NGC 4552 was measured via its surface brightness fluctuations, its luminosity distance proved to be comparable to that of M87. From the comparison of the sight velocities of these two galaxies, the velocity of M89's movement through the ICM is supersonic with the value of $\Delta v_r = -967 \pm 11$ km/s towards us relative to M87 (Machacek, Nulsen, Jones & Forman 2006). Therefore, we can conclude that M89 is experiencing ram-pressure stripping.

The evidence of this is also seen in the X-ray observations of the galaxy. Many distinct features can be attributed to ram-pressure stripping, specifically a sharp surface brightness profile at 3.1 kpc from the center, a stretched tail of galaxy gas stretching 10 kpc behind the galaxy, and two horn like structures with a prominent cold front extending 3 to 4 kpc to either side of the galaxy. These structures are further analysed in detail in Machacek, Nulsen, Jones & Forman (2006) and revised in Kraft et al. (2017).

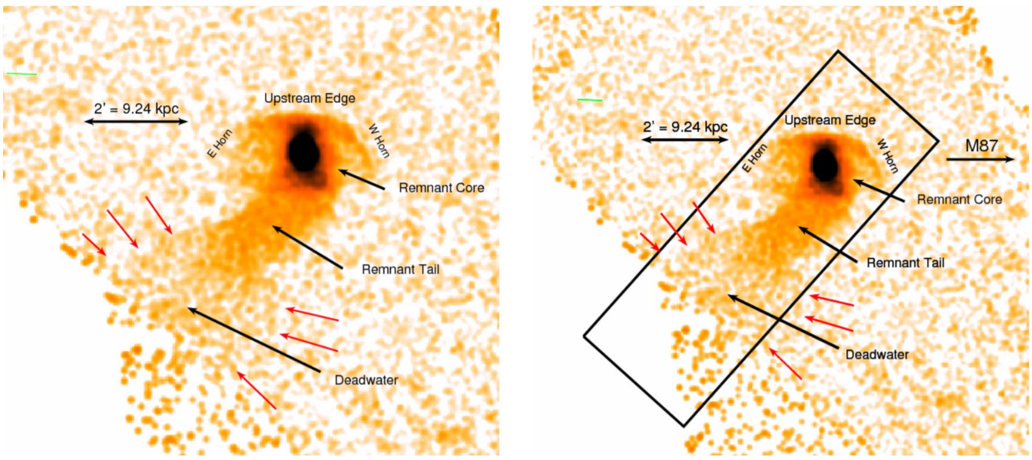

Figure 3.2: Exposure corrected Chandra image of M89 in the energy range of 0.7-1.1 keV. Key labelled features include the dense unstripped gas at the center (the remnant core), the region of unstripped gas from the halo shielded by the remnant core (the remnant tail), and the region of stripped gas that is mixing with the ICM (the deadwater region). Taken from Kraft et al. (2017).

However, Kraft et al. (2017) admit that the appearance of these features heavily depends on their history and cannot be sufficiently examined without the context of their creation. They admit that the two horn-like structures and the remnant tail could also be remnant shocks created by an earlier AGN outburst which expelled part of the galaxy's atmosphere, and the morphology of the gas lost its symmetry due to the ram-pressure forces exhibited by the infall of NGC 4552 into the Virgo cluster.

3.2 Presence of AGN

In chapter 2 we focused on AGNs and their affect on their host galaxies. As expected, galaxy NGC 4552 is itself a host to an AGN, whose presence was strongly indicated by studies of NGC 4552's nuclear properties across a wide range of wavelengths (see Machacek, Jones, Forman & Nulsen 2006). The brightness temperature of $T_{\rm B} = 2 \times 10^9$ K at 5 GHz was measured. This value is too high for either a nuclear outburst or collection of supernova remnants and its shape of radio emission spectrum is too flat for either of these categories. The mass of the central black hole was extrapolated using the correlation between its mass and the central velocity dispersion to be $4 \times 10^8\ M_\odot$. Therefore, these studies suggest that M89 is hosting a weak AGN with a LINER classification at its center, which can be considered one of the faintest AGN observed.

Furthermore, NGC 4552 also showcases structures indicating an outburst of its central AGN. These features are two rings of shocked gas in the central region of the galaxy. They are approximately circular and of equal size, creating a distinct 'hourglass' appearance. Such formations are present in other galaxies as well, documenting past outbursts of the supermassive black hole. According to Machacek, Jones, Forman & Nulsen (2006), these features are consistent with bipolar nuclear outflow cavities, which can be found $\sim$1.3 kpc away from the centre of the galaxy with a temperature of $\sim 0.61 \pm 0.02$ keV. From the shape of the surface brightness profile, they have estimated that the rim of the rings is consistent with a simple spherical model for a Mach 1.7 shock caused by a nuclear outburst with the power of 1.4×10^{55} ergs which happened about 1 to 2 Myr ago.

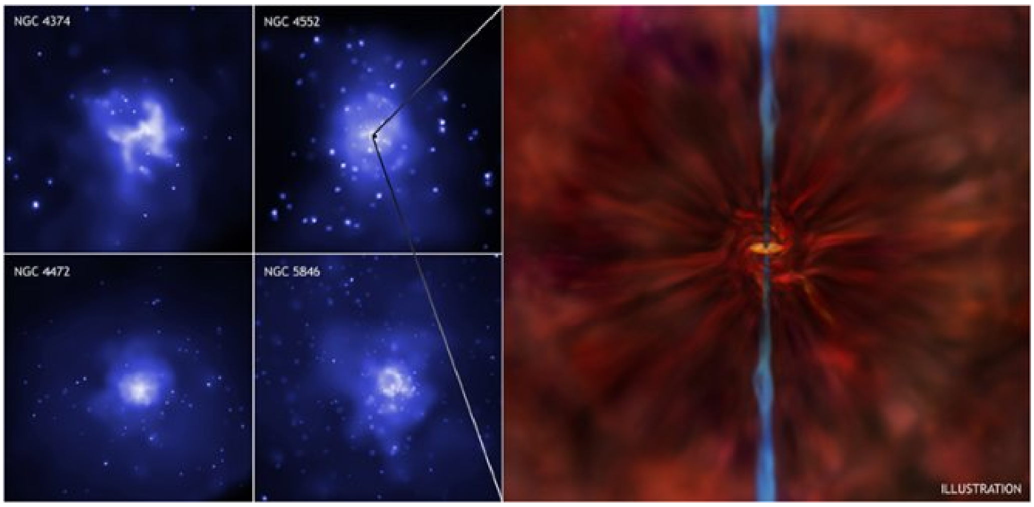

Figure 3.3: (*left*) Images of four supermassive black holes captured by the CXO and (*right*) an artist's impression of the black hole found in the center of NGC 4552. It showcases gas falling into the supermassive black hole, one fraction joining an accretion disc while the other is being swept upwards into jets. Credit: NASA/CXC & Weiss (2008)

Chapter 4

Data and analysis

4.1 Chandra

Chandra X-ray Observatory (CXO) is a telescope operated by NASA designed to detect X-ray emission ”from very hot regions of the Universe such as exploded stars, clusters of galaxies, and matter around black holes” as stated on their website (SAO 2021). Chandra is orbiting the Earth along highly elliptical orbit with the furthest point reaching an altitude of 139 000 km. Chandra’s orbit allows it to observe continuously up to 55 hours of its 65-hour long orbital period.

One of the most important parts of the telescope itself is the system of mirrors. Those used in X-ray telescopes must be very different from those found in optical telescopes because of the high energy photons they redirect. In optical telescopes simple parabolic mirrors coated in aluminium foil are used, while X-ray telescopes are made of nested cylindrical paraboloid and hyperboloid surfaces coated with iridium or gold (known as Wolter type I configuration shown in Figure 4.1 (a)) to achieve a low grazing angle necessary to reflect X-ray photons.

The Chandra telescope system consists of four pairs of mirror shells, their support structure, and a number of X-ray and thermal baffles called the High Resolution Mirror Assembly (HRMA for short) as seen in Figure 4.1 (b). The substrate of the mirrors is a 2 cm thick glass whose reflective surface is coated with a 33 nm iridium layer. The diameters of the four shells are 65 cm, 87 cm, 99 cm and 123 cm. The thick substrate and careful polishing to the smoothness of a few atoms gives Chandra a very precise optical surface, allowing it to have unparalleled resolution of less than $1''$and FOV of $30'$ (Gaetz & Jerius 2004).

The mirrors focus the incoming X-ray photons on an area of approximately 40 μm^2 on the focal plane, which is situated 9 m away from the mirrors. In this area science instruments ACIS and HRC can be found, which provide the information about the number, position, energy and time of arrival of captured X-ray photons. ACIS includes 10 CCD chips divided

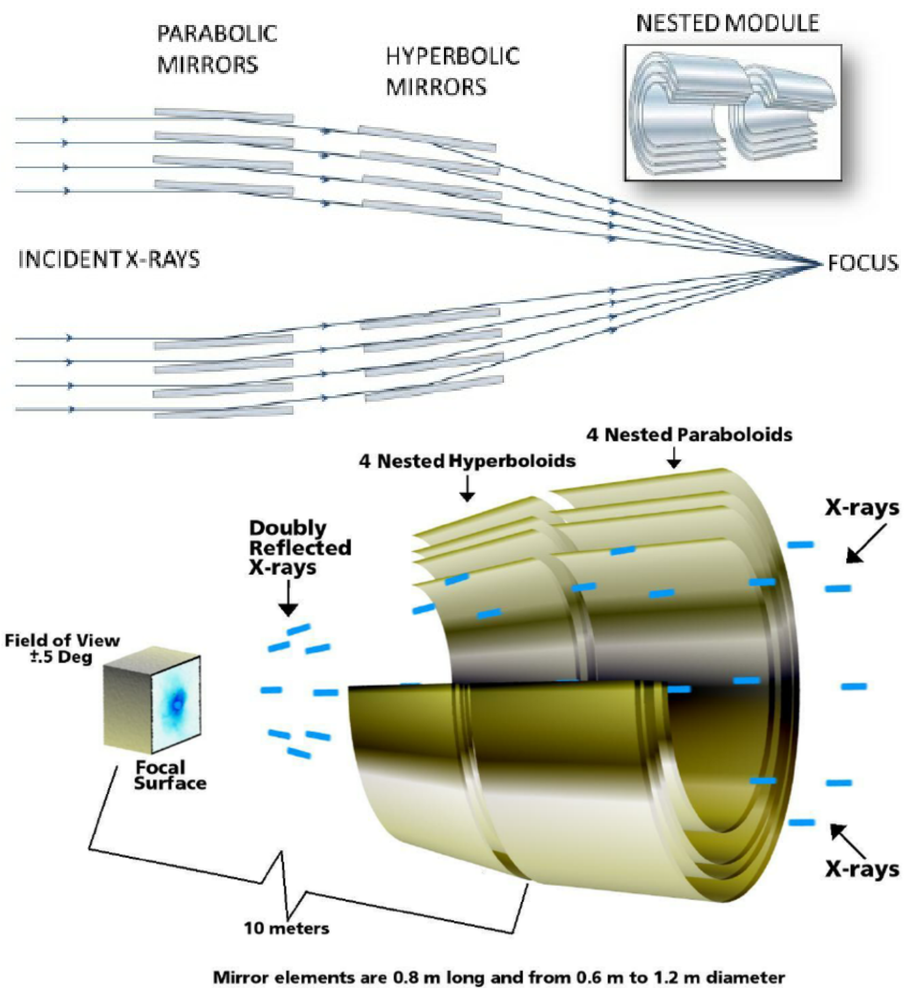

Figure 4.1: (*a*) Schematic of a Wolter Type I configuration. In order to focus the incoming X-ray photons, they are once reflected off of a parabolic surface and afterwards off of a hyperbolic surface. (*b*) Schematic of the Chandra X-ray Observatory's mirror system of four nested, co-axial, confocal, grazing-incidence mirror pairs.

into two categories; ACIS-I, and ACIS-S, where both provide imaging and spectroscopic information of the object observed. Both parts operate in the energy range of 0.2 - 10 keV. HRC, compared to the ACIS unit only provides the imaging infromation, and consists of two micro-channel plate components running in the energy range of 0.1 - 10 keV.

Additionally, Chandra carries two other instruments which provide highly detailed information about X-ray energy, the LETG and HETG spectrometers. When these grating arrays are used, they diffract the photons depending on their energy. Their position is measured by either HRC or ACIS, so that the exact energy can be determined (SAO 2019).

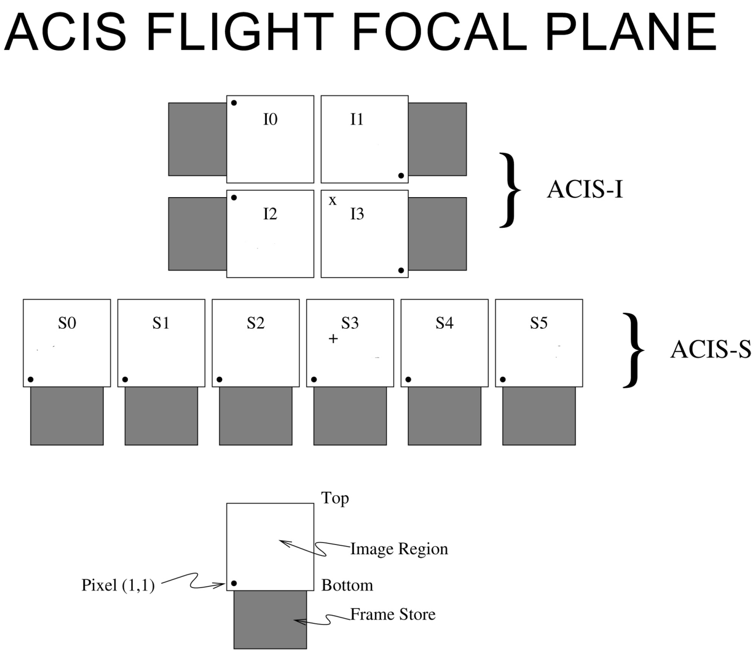

Figure 4.2: Schematic of the ACIS chip layout aboard CXO.

4.2 Data analysis

For our thesis, we used a total of ~201 ks observation of the eliptical galaxy M89 found in the Virgo cluster taken with Chandra in 2003 and 2012 (ObsID 2072, 13985, 14358, 14359) using the Advanced CCD Imaging Spectrometer array with ACIS-S (chip S3) at the aim-point. All four observations were reprocessed using CIAO 4.12.

4.2.1 Imaging analysis

For our imaging analysis we began by reprocessing each data set using the latest gain tables and instrumental corrections, which included correction for charge transfer inefficiency (CTI), time-dependent gain (tgain) adjustment of the ACIS chip, while filtering events with significant flux in border pixels of the 5×5 event island (VFAINT) that could be attributed to cosmic rays, which cleans the ACIS particle background. Afterwards, we deflared each data set, resulting in observation time of 199.957 s. From the estimated distance of the galaxy, we have determined that $1''$corresponds to a distance scale of 77 pc.

Following the reprocessing and filtering, we reprojected each observation to the same tangent point, limiting data only to the S3 chip, because the desired area of M89 which we wish to study does not overlap to other chips. These reprojected event files were then merged and exposure-corrected using energy range of 0.5 to 2.0 keV and exposure-map energy of 0.92 keV, best suited for objects emitting in the soft band, which fits our galaxy.

For the backgrounds we ran the *blanksky* script for each observation and the created *blanksky* background files were then reprojected to the same tangent point, and explicitly filtered on the same energy range as the merged event data while also rebinned to the correct image size. Afterwards, the *blanksky* files were each scaled by their individual scaling factor and merged into one background file which was also exposure corrected. This final scaled and exposure-corrected background file was then subtracted from our initial merged image file. Point sources were identified using the *wavdetect* algorithm and subsequently removed, and the remaining regions were filled with Poisson distribution of the pixel values in the background region using CIAO tool *dmfilth*.

The final Chandra X-ray image of NGC 4552 in the 0.5-2.0 keV band is shown in Figure 4.3 with the diffuse emission from the two ring-like structures in the central region of M89. The two rings are nearly circular and of equal size. We have estimated the inner radius of the rings to be ∼12″and the outer to be ∼17″ which corresponds to 0.90 kpc and 1.29 kpc.

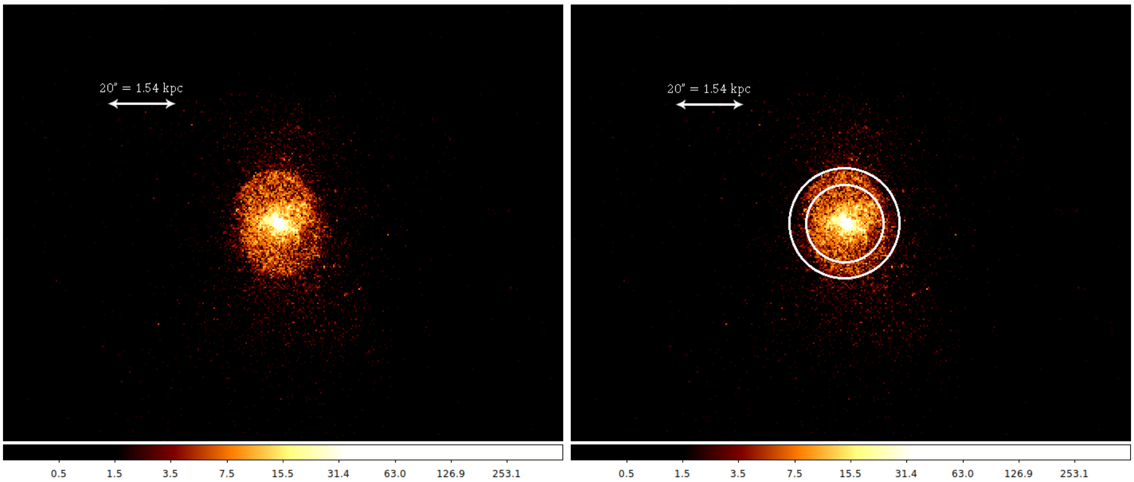

Figure 4.3: (*left*) Background subtracted Chandra X-ray image of the 0.5-2.0 keV diffuse emission showcasing the two ring-like structures in the central region of NGC 4552. (*right*) Chandra image of the same region, with the two radii of the shock front indicated with white circles. Both colour bars are in the units of phot cm^{-2} s^{-1} arcsec^{-2} in the energy range of 0.5-2.0 keV.

4.2.2 Spectral analysis

We began spectral analysis by creating various extraction source and background regions on the event files for each observation. In order to substantially compare our results with the results of Machacek, Jones, Forman & Nulsen (2006), we used the source and background regions listed in this paper. We subsequently checked the differences in the fitted spectra of the northern and southern ring, and found no significant differences between these two structures. Therefore we continued with the single annular region for the shock rim. Additionally, we created three other regions; circular region with radius of 10 kpc, an annular region outside of the shock ring and an annular region inside of the shock ring. We list all regions used in Table 4.1 and shown in Figure 4.4. Before extracting the spectra, we reprojected each data set to a common tangent point, deflared the data as in subsection 4.2.1, and removed all visible point sources.

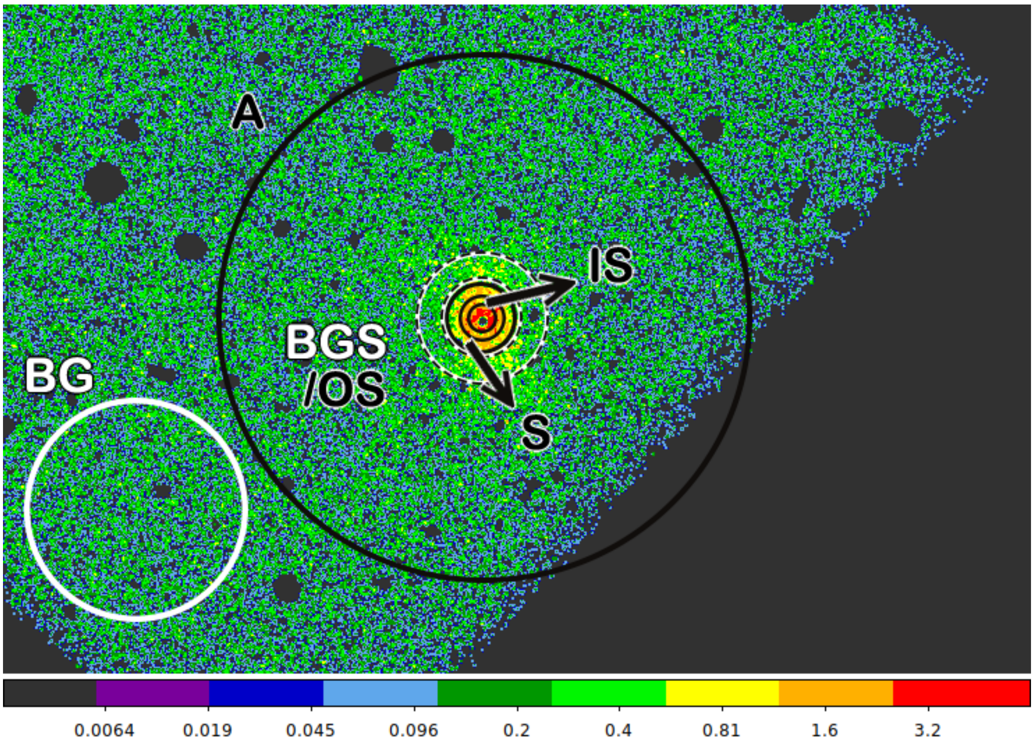

Figure 4.4: Chandra X-ray image of the galaxy M89 from ObsID 13985 with point sources removed with regions of extracted spectra denoted. The white circles belong to the background regions (*BG – background, BSG – shock background*), while the black ones show the source regions (*A – all, S – shock, IS – inside shock, OS – outside shock*). The region for the outside-shock source overlaps with the background region for the shock.

Table 4.1: Spectral analysis regions of NGC 4552

Region	Type	Shape	Centre [RA, DEC]	Dimensions [arcsec]
A	source	circular	12:33:08.24, +12:49:54.31	130
BG	background	circular	12:35:51.35, +12:31:50.15	55
IS	source	annular	12:33:08.27, +12:49:53.83	7; 10
S	source	annular	12:33:08.29, +12:49:53.39	11; 17
BGS	background	annular	12:33:08.29, +12:49:53.39	20; 31
OS	source	annular	12:33:08.29, +12:49:53.39	20; 31

NOTE: All WCS coordinates for the centres are J2000. The specified dimensions are radii for circular regions, and (inner, outer) radii for annular regions. All regions are shown in Figure 4.4.

With the regions and data sets prepared, we started extracting spectra from the observations provided by Chandra's S3 chip with CIAO's function *specextract*. Because spectra cannot be extracted from the merged event file, we proceeded to run the script on each observation. After creating a spectrum for each individual data set, we combined them using the *combine_spectra* command, allowing us to analyse spectra with higher count rate.

For the analysis below, since the emitted X-rays of M89 are in the soft band, we restricted all spectral fit energy ranges to 0.5-2.0 keV, where the source count rates are above background emission. Using Sherpa, CIAO's extension for modelling and fitting spectra, a single temperature VAPEC model with Galactic absorption fixed at the value $n_{\mathrm{H}} = 2.67 \times 10^{20}$ cm^{-2} (HEASARC 2019*b*), and redshift value of $z = 0.00113$ (HEASARC 2019*a*) was used in all regions. We use Chi-square statistic and applying the Levenberg-Marquardt nonlinear least-squares algorithm. The temperature and elemental abundances of O, Fe, Si, Mg, and Ne were left as free parameters in all fits, all other abundances were fixed at Solar value. We used a VAPEC model instead of an APEC model, which was used by (Machacek, Jones, Forman & Nulsen 2006), because the emission lines of Fe, O, and Si dominate the spectra in the temperature range of interest (0.5-2.0 keV), and as stated in Kraft et al. (2017) "scaling them all by a constant factor (i.e. using the APEC model rather than the VAPEC model) would introduce a systematic error in both the density and temperature measurements of the spectral fits."

The best fit VAPEC model spectral parameters (68% confidence) for each region are listed in Table 4.2. The elemental abundances of the 10 kpc region A were measured to be 0.37, 0.29, 0.40, 0.54, and 0.21 times the Solar value for O, Ne, Mg, Si, and Fe, respectively, while the temperature reached the value of 0.61 keV. Because our primary goal is to inspect the shock rim, we mainly focus on the region S and OS. When looking at the edge of the shock rings, we find that the abundances of O, Ne, Mg, and Fe are doubled compared to those outside of the shock ring, while the abundance of Si stays relatively unchanged. The apparent hint of increase in abundances of O and Ne could be caused by the intricate temperature structure of the shock region and the statistical model compensating for these changes.

Table 4.2: Spectral models of NGC 4552's regions

Region	A	IS	S	OS
kT [keV]	0.61±0.01	0.70±0.02	0.72±0.02	0.48±0.05
O [$Z_{\odot}$]	0.37±0.08	0.26±0.24	0.59±0.30	0.24±0.21
Ne [$Z_{\odot}$]	0.29±0.08	0.53±0.35	1.04±0.45	0.53±0.32
Mg [$Z_{\odot}$]	0.40±0.07	0.81±0.27	0.82±0.28	0.54±0.36
Si [$Z_{\odot}$]	0.54±0.10	0.58±0.20	0.64±0.24	0.68±0.45
Fe [$Z_{\odot}$]	0.21±0.02	0.37±0.08	0.48±0.11	0.26±0.09
norm [10^{-4}]	7.78±0.63	0.57±0.11	0.71±0.14	0.55±0.15

NOTE: Spectral model parameters for each region specified in Table 4.1 and depicted in Figure 4.4, using a single temperature VAPEC model with Galactic absorption fixed at the value $n_{\mathrm{H}} = 2.67 \times 10^{20}$ cm^{-2} (HEASARC 2019*b*) over the 0.5-2 keV energy range. Parameters are fitted within 68% confidence limits.

The temperature at the rim of the shock and ambient gas drops from (0.72 ± 0.02) keV to (0.48 ± 0.05) keV just outside the rim. This shows us that the temperature in the bright rims in region S is higher than the temperature of the outside region in region OS. As stated in Machacek, Jones, Forman & Nulsen (2006), this is in contrast with the properties of a cold front created by ram pressure, where the brighter region has cooler temperature than its darker surroundings, or the vivid edges of highly evolved remnant cavities from nuclear activity. Our observations are consistent with the observed properties of shocks driven into the surrounding gas from recent AGN outbursts, as in, for example, Hydra A shown in Nulsen et al. (2005). We have verified that the temperature rise is not a result of unresolved X-ray binaries by fitting a bremsstrahlung component at 7.3 keV (Irwin et al. 2003) over the energy range of 0.3 - 8 keV in region S. The resulting best fit temperature of (0.72 ± 0.02) keV agrees with the previous result, therefore the effects of unresolved X-ray binaries on our data are insignificant.

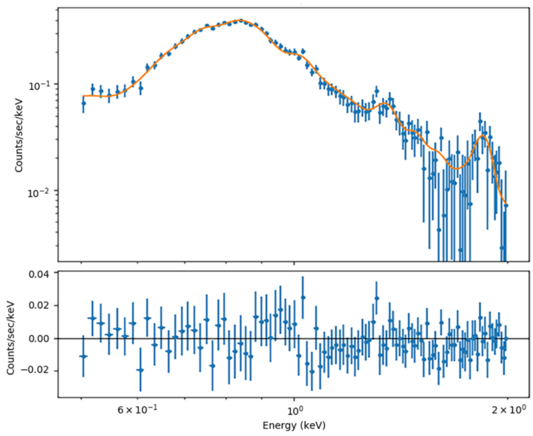

(a) Spectral fit of region A of NGC 4552.

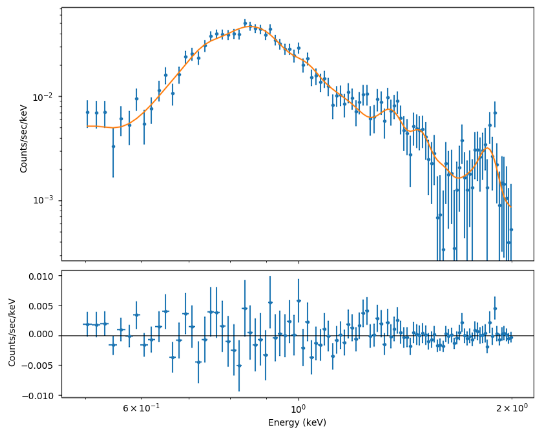

(b) Spectral fit of region OS of NGC 4552.

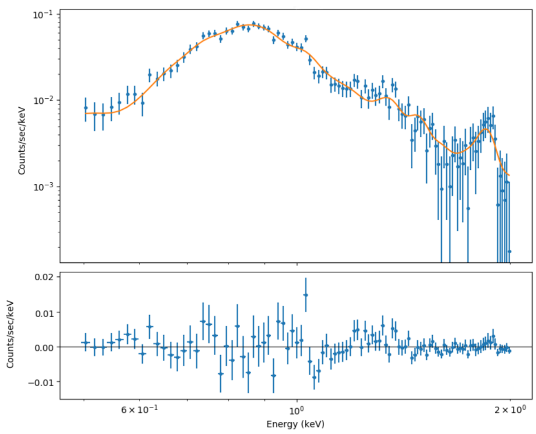

(c) Spectral fit of region S of NGC 4552.

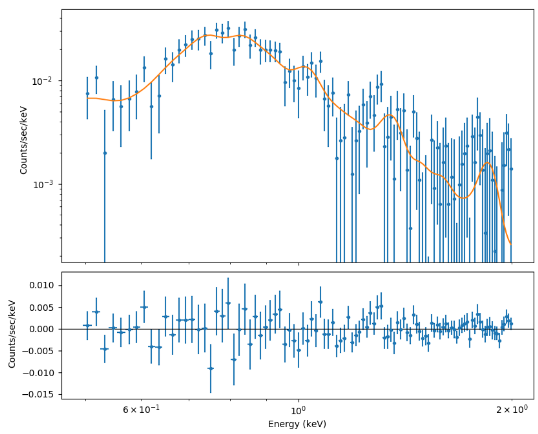

(d) Spectral fit of region OS of NGC 4552.

Figure 4.5: Spectral fit of a single temperature VAPEC model with Galactic absorption for each region specified in Table 4.1 and depicted in Figure 4.4 over the 0.5-2 keV energy range.

Comparing our resulting values of temperatures to those obtained by Machacek, Jones, Forman & Nulsen (2006), we can clearly see some differences, specifically in the temperature of the shock rings. Our value of (0.72 ± 0.02) keV is higher by 0.08 keV, and this difference is not included in either ours or previous researcher's uncertainties. Differences can be found in the temperature of the ambient gas as well, with these reaching value of 0.05 keV. We conclude that these variances were caused by two factors, mainly the systematic error introduced by the used APEC model with contributions of lower data count compared to our research.

4.2.3 Surface brightness analysis

Another analysis which we conducted on our data was the modelling of surface brightness profile for galaxy M89, in particular to determine the density compression factor found at the shock rim. For this analysis we used the exposure-corrected image with the energy of 0.5-2.0 keV, which we described in detail in subsection 4.2.1, a PSF map, and a scaled blanksky background file created in the same process. After loading these files into the data structure of the python package *pyproffit* (Eckert 2020), we masked the detected point sources, which were found using the *wavdetect* algorithm, to avoid contaminating the profile.

By defining a circular region of $5'$ with the centre choice in the luminosity peak with equatorial coordinates of $\alpha = 12^{\mathrm{h}}\ 35^{\mathrm{m}}\ 39.8^{\mathrm{s}}$ and $\delta = 12^{\circ}\ 33'\ 22.1''$, we extracted a surface brightness profile from our data with the binning set to the smallest component possible. Using the equation for spherically symmetric broken power law presented in section 2.3, we defined a model for double broken power law to accommodate the two discrepancies in the surface brightness; one at the shock rim, which is the area of our main focus, and another one at the cold front, which is a structure similar to shock rims in appearance, however the gas found here has lower temperature and entropy than the hotter ambient gas. Cold fronts are described in more detail and analysed by both Machacek, Nulsen, Jones & Forman (2006) and Kraft et al. (2017).

We extracted the surface brightness profile from an annular region with inner radius of 0.5 kpc and outer radius of 13.5 kpc in order to capture both gas density discrepancies and to compare the shock speed calculated via temperature ratio extracted from spectral analysis, while also recreating the entire annular surface brightness profile for galaxy M89. The best fit parameters of the broken power law parameters expanding over this region are shown in Table 4.3. From this model using the χ^2 minimization, we find the best fit position for the discontinuity in surface brightness across the rim of the shock ring shown in Figure 4.6 at $r_{\mathrm{rim}} = (16.9 \pm 0.1)''$or (1.30 ± 0.01) kpc, coincident with the edge of the outer rim of the shock ring, which we extrapolated from Figure 4.3. For the electron density in the area of $r > r_{\mathrm{rim}}$ we find the slope to be $\alpha_1 = 0.63 \pm 0.04$, while the slope for the electron density outside of the shock ring has the value of 1.41 ± 0.03. We also fitted over the area of the cold front, with the best fit for its edge to be at 3.84 kpc.

Table 4.3: Surface brightness profile model over an angular region of NGC 4552

Parameter	Value
α_1	0.63 ± 0.04
α_2	1.41 ± 0.03
α_3	1.60 ± 0.03
r_{rim1} [$'$]	0.282 ± 0.002
r_{rim2} [$'$]	0.832 ± 0.060
norm_1	-2.56 ± 0.02
norm_2	-4.26 ± 0.02
jump_1	1.73 ± 0.05
jump_2	1.59 ± 0.05
bkg	-5.50 ± 0.06

NOTE: Surface brightness profile model parameters for NGC 4552, using a double broken power law model over the 0.5-2 keV energy range. Parameters are fitted within 68% confidence limits.

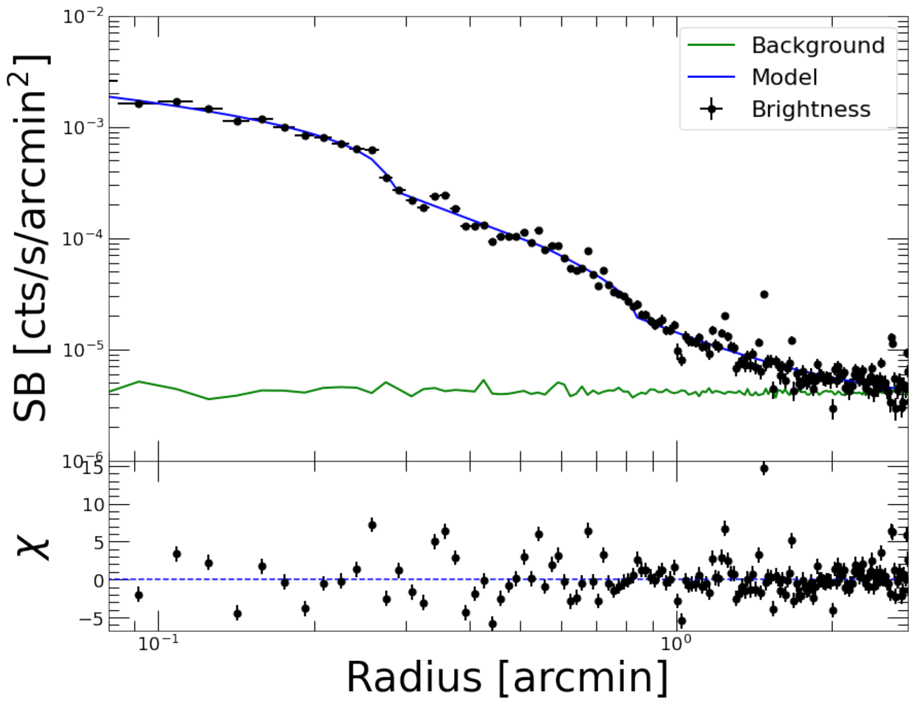

Figure 4.6: Surface brightness profile model fitted over an annular region of $0.46 > r > 13.86$ kpc. The convert rate between angular distance and regular is $1'' = 77$ pc.

However, as stated in Machacek, Jones, Forman & Nulsen (2006): "since the shock front is narrow, the averaged, measured surface brightness discontinuity will underestimate the actual density discontinuity at the narrow shock front, and thus also the inferred shock strength and temperature rise". Therefore, we cannot use the whole annulus for a precise measurement of the gas discrepancy found in the galaxy. Thus, we have compared the surface brightness profiles of the two rings across the shock front (Figure 4.7) and found only slight variances in the luminosity. By normalizing the surface brightness profile of the southern ring, we managed to better compare the shape of the jump in luminosity and found that it agrees within errors for both rings. Hence we use the northern ring (angular sector spanning from 64° to 121°) as representative of both rings.

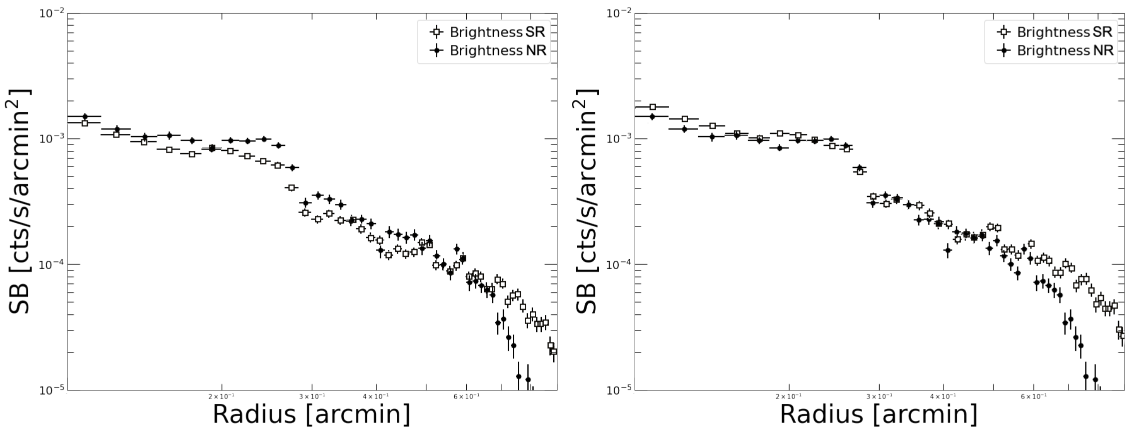

Figure 4.7: (*left*) The 0.5-2 keV surface brightness profile over the northern (circles) and southern (squares) rings taken in angular sectors of 64° to 121° for northern edge and 257° to 349° for the southern edge. Measured counter-clockwise from Figure 4.3. (*right*) Illustration of the near match of the surface brightness jump across both rings by normalizing the surface brightness profile of the southern wedge. We only find a small difference.

After performing the surface brightness profile extraction and modelling of a single broken power law focusing on region $0.46 > r > 2.77$ kpc within, we find the best fit position for the discontinuity in surface brightness across the edge of the shock shown in Figure 4.8 at $r_{\rm rim} = (17.5 \pm 0.1)''$or (1.35 ± 0.01) kpc, also coincident with the edge of the outer rim of the shock ring established with imaging analysis and surface brightness profile of the entire annulus. For the electron density we find changes from the previous results, seeing as the slope in the area of $r > r_{\rm rim}$ is $\alpha_1 = 0.10 \pm 0.01$, while the slope for the electron density outside of the shock ring reaches 1.45 ± 0.05. Therefore, we conclude that using the entire annular region introduced significant errors into our analysis, and we only use those results for comparison with the spectral analysis.

Table 4.4: Surface brightness profile model over the northern ring of NGC 4552

Parameter	Value
α_1	0.10 ± 0.01
α_2	1.45 ± 0.05
$r_{\rm rim}$ [$'$]	0.292 ± 0.001
norm	-2.39 ± 0.03
jump	1.82 ± 0.09
bkg	-5.50 ± 0.06

NOTE: Surface brightness profile model parameters or angular sector over the northern ring for NGC 4552, using a broken power law model over the 0.5-2 keV energy range. Parameters are fitted within 68% confidence limits.

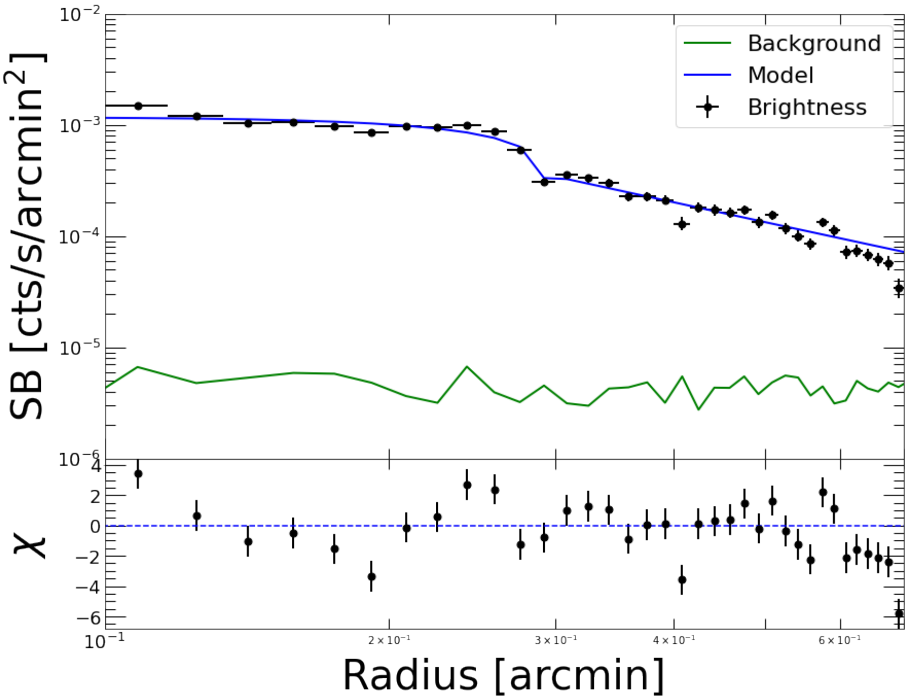

Figure 4.8: Surface brightness profile model fitted over an angular region of 64° to 121° . The convert rate between angular distance and regular is 1″= 77 pc.

4.2.4 Shock analysis

Using both spectral and surface brightness analysis, we are now able to estimate the speed of the nuclear outflow seen as a shock rim at the radius $r \sim 1.3$ kpc in NGC 4552.

First and foremost, we focus on the temperature discontinuity found using spectral analysis. Assuming that the adiabatic index of the shocked gas is $\gamma = 5/3$ estimated from the

Rankine-Hugoniot shock conditions (section 2.3) and $T_{\rm rim}/T_{\rm out} = 1.51 \pm 0.16$, we are able to estimate the shock speed (Mach number M_1) of the gas using Equation 2.8 as $M_1 = 1.52 \pm 0.08$. Now we can compare this result using the compression ratio or the "jump" parameter used to estimate gas density jump over an annular region as shown in Figure 4.6 and discussed in detail in subsection 4.2.3. Using Equation 2.7, and the value of jump $= 1.73 \pm 0.05$, we calculate the speed of shock to be $M_1 = 1.51 \pm 0.03$. This value is equivalent to the one estimated from the same region via spectral analysis.

Now we turn to the gas discrepancy found via the more precise surface brightness extraction from an angular section spanning over the northern ring of the shock front. Using the compression ratio found using the broken power law model of jump $= 1.82 \pm 0.09$, Equation 2.7 gives us a value of $M_1 = 1.58 \pm 0.04$ for the northern shock ring.

Comparing our result obtained via spectral analysis with Machacek, Jones, Forman & Nulsen (2006)'s value of $T_{\rm rim}/T_{\rm out} = 1.48 \pm 0.14$, we find that these two values are almost identical, deviating only by 0.04 keV, which is well within our and previous uncertainties. Therefore, we conclude that despite the preceding research having a systematic error in the measurements of temperature caused by the APEC model, it does not affect the value of temperature ratio needed to calculate the Mach number, as the error seemingly neutralises itself in these calculations. However, we find slight differences in Mach numbers when using the surface brightness profile of the northern ring. While previous research estimated its value to be 1.7 ± 0.2, our model points to a lower value of 1.58 ± 0.04, though our value is included in the uncertainty of the previous research. We therefore conclude that our analysis proved to be more precise because of the larger dataset used for our research. Moreover, when comparing the results obtained via different methods, the values of the shock speed do not deviate as such as those found in the preceding research.

Conclusion

The purpose of our work was to focus on the elliptical galaxy NGC 4552 and its ring-like structures, whose presence was attributed to an AGN outburst by previous studies. Our goal was to re-analyse these structures with more data available and determine whether earlier research arrived at correct conclusions, and update any differences we may have found.

In chapter 1, we introduced the topic of hot atmospheres. We at first explained the nature of this phenomenon, and described its properties found by previous observations and studies. Afterwards, we focused on their emission in X-ray, the process responsible for this emission and what these spectra can unveil about hot atmospheres permeating galaxy clusters. With the properties of ICM explained, we moved on to the phenomena alternating the uniformity of the gas and the physics behind the changes seen in the hot gas. These phenomena include the infall of galaxies through the atmosphere and the outburst of active galactic nuclei. For that reason, we described active galactic nuclei in chapter 2. In this chapter we elucidated the nature of AGNs and briefly summarised how the supermassive black holes located at the centres of active galaxies can release energy back into the ICM. This led us to also touch upon the topic of star formation and what effect an AGN has on it. Seeing as the presence of AGNs can create many distinct structures, e.g. shock fronts, we also explained the physics behind these occurrences, as well. The most important feature we touched upon was the speed of the shock or Mach number M_1 which we set out to find for galaxy NGC 4552 using different techniques.

With the theoretical part concluded, we moved on to describe the object of our interest, galaxy NGC 4552. First, we outlined the general properties of the galaxy, including but not limited to its position in the night sky and within the Virgo cluster, the history of its discovery, and its shape and distinct features present in the visible band. Afterwards we moved on to describe structures of M89 which were discovered by X-ray studies of this galaxy. One of these structures is a ram-pressure stripped tail, which is closely analysed by Machacek, Nulsen, Jones & Forman (2006) and later revised by Kraft et al. (2017), and briefly described by us in section 3.1. Furthermore, we moved on to the main focus of our study, the remnant shock rings found by a previous detailed X-ray study of the galaxy. Because the most recent observations of this galaxy were done using the *Chandra X-ray Observatory*, and we used data from this satellite as well, the properties, concepts on which CXO operates, and instruments aboard were introduced in section 4.1.

After thoroughly summarising the previous research done about the ring-like structures of M89, and introducing the instrument used to collect the data used, we started the practical part of our thesis. We analysed 199.957 ks *Chandra* observations of an elliptical galaxy NGC 4552 in the Virgo cluster. We reviewed the X-ray evidence of remnant shocks from recent AGN activity found in the inner region of the galaxy. By imaging analysis we confirmed the position of the two ring-like structures to be at $r \sim 1.3$ kpc from the centre of M89, which is consistent with findings by Machacek, Jones, Forman & Nulsen (2006), and further confirmed this position via surface brightness profile modelling. Next we used both surface brightness profile model and spectral fitting to find the speed of the shock. Through spectral analysis we found the temperature ratio to be $T_{\text{rim}}/T_{\text{out}} = 1.51 \pm 0.16$ which corresponds to a Mach 1.5 shock. The surface brightness profile model across the edge of the shock of the northern ring gave us the density ratio od $n_{\text{rim}}/n_{\text{out}} = 1.82 \pm 0.09$ which is consistent with a simple spherical model for a Mach 1.6 shock. Comparing our results with those provided by Machacek, Jones, Forman & Nulsen (2006), we conclude that our analysis proved to be more precise because of the larger dataset used in this research, as suggested by lower deviancy in the values of the Mach number estimated by different methods compared to the preceding study.

Bibliography

Abramson, A., Kenney, J., Crowl, H. & Tal, T. (2016), 'HST Imaging of Dust Structures and Stars in the Ram Pressure Stripped Virgo Spirals NGC 4402 and NGC 4522: Stripped from the Outside in with Dense Cloud Decoupling', *The Astronomical Journal* **152**(2), 32.
URL: *http://dx.doi.org/10.3847/0004/6256/152/2/32*

Böhringer, H., Briel, U. G., Schwarz, R. A., Voges, W., Hartner, G. & Trümper, J. (1994), 'The structure of the Virgo cluster of galaxies from ROSAT X-ray images', *Nature* **368**(6474), 828–831.
URL: *https://ui.adsabs.harvard.edu/abs/1994Natur.368..828B*

Bykov, A. M., Churazov, E. M., Ferrari, C., Forman, W. R., Kaastra, J. S., Klein, U., Markevitch, M. & de Plaa, J. (2015), 'Structures and Components in Galaxy Clusters: Observations and Models', *Space Science Reviews* **188**(1-4), 141–185.
URL: *http://dx.doi.org/10.1007/s11214-014-0129-4*

Cavaliere, A. & Fusco-Femiano, R. (1976), 'X-rays from hot plasma in clusters of galaxies.', *Astronomy and Astrophysics* **500**, 95–102.

Clark, G., Plucinsky, P. & Ricker, G. (1987), *The "Jet" of M89 : CCD Surface Photometry*, Vol. 127.

Eckert, D. (2020), '*Pyproffit*'. [Accessed: 12.03.2021].
URL: *https://pyproffit.readthedocs.io/en/latest/intro.html*

Fabian, A. (2012), 'Observational Evidence of Active Galactic Nuclei Feedback', *Annual Review of Astronomy and Astrophysics* **50**(1), 455–489.
URL: *http://dx.doi.org/10.1146/annurev-astro-081811-125521*

Frommert, H. & Kronberg, C. (2007), '*Messier 89*'. [Accessed: 23.03.2021].
URL: *http://www.messier.seds.org/m/m089.html*

Gaetz, T. & Jerius, D. (2004), '*The HRMA User's Guide*'. [Accessed: 13.05.2021].
URL: *https://cxc.harvard.edu/ccw/proceedings/2004/presentations/gaetz/gaetz.pdf*

Gaspari, M., Ruszkowski, M. & Oh, S. P. (2013), 'Chaotic cold accretion on to black holes', *Monthly Notices of the Royal Astronomical Society* **432**(4), 3401–3422.
URL: *http://dx.doi.org/10.1093/mnras/stt692*

Gunn, J. E. & Gott, J. Richard, I. (1972), 'On the Infall of Matter Into Clusters of Galaxies and Some Effects on Their Evolution', *The Astrophysical Journal* **176**, 1.

Harrison, C. M. (2017), 'Impact of supermassive black hole growth on star formation', *Nature Astronomy* **1**, 0165.

HEASARC (2019*a*), '*Detailed Information for a Named Object*'. [Accessed: 23.05.2021].
URL: *https://ned.ipac.caltech.edu/?q=byname&objname=NGC%204552*

HEASARC (2019*b*), '*nH*'. [Accessed: 19.05.2021].
URL: *https://heasarc.gsfc.nasa.gov/cgi-bin/Tools/w3nh/w3nh.pl*

Irwin, J. A., Athey, A. E. & Bregman, J. N. (2003), 'X-Ray Spectral Properties of Low-Mass X-Ray Binaries in Nearby Galaxies', *The Astrophysical Journal* **587**(1), 356–366.
URL: *http://dx.doi.org/10.1086/368179*

Janowiecki, S., Mihos, J. C., Harding, P., Feldmeier, J. J., Rudick, C. & Morrison, H. (2010), 'Diffuse Tidal Structures in the Halos of Virgo Ellipticals', *The Astrophysical Journal* **715**(2), 972–985.
URL: *http://dx.doi.org/10.1088/0004-637X/715/2/972*

Kraft, R. P., Roediger, E., Machacek, M., Forman, W. R., Nulsen, P. E. J., Jones, C., Churazov, E., Randall, S., Su, Y. & Sheardown, A. (2017), 'Stripped Elliptical Galaxies as Probes of ICM Physics. III. Deep Chandra Observations of NGC 4552: Measuring the Viscosity of the Intracluster Medium', *The Astrophysical Journal* **848**(1), 27.
URL: *http://dx.doi.org/10.3847/1538-4357/aa8a6e*

Machacek, M., Jones, C., Forman, W. R. & Nulsen, P. (2006), 'Chandra Observations of Gas Stripping in the elliptical galaxy ngc 4552 in the virgo Cluster', *The Astrophysical Journal* **644**(1), 155–166.
URL: *http://dx.doi.org/10.1086/503350*

Machacek, M., Nulsen, P. E. J., Jones, C. & Forman, W. R. (2006), 'Chandra Observations of Nuclear Outflows in the Elliptical Galaxy NGC 4552 in the Virgo Cluster', *The Astrophysical Journal* **648**(2), 947–955.
URL: *http://dx.doi.org/10.1086/505963*

Malin, D. F. (1979), 'A Jet Associated with M89', *Nature* **277**(5694), 279–280.

McNamara, B. R. & Nulsen, P. E. J. (2012), 'Mechanical feedback from active galactic nuclei in galaxies, groups and clusters', *New Journal of Physics* **14**(5), 055023.
URL: *http://dx.doi.org/10.1088/1367-2630/14/5/055023*

McNamara, B. R., Russell, H. R., Nulsen, P. E. J., Hogan, M. T., Fabian, A. C., Pulido, F. & Edge, A. C. (2016), 'A Mechanism For Stimulating AGN Feedback by Lifting Gas in Massive Galaxies', *The Astrophysical Journal* **830**(2), 79.
URL: *http://dx.doi.org/10.3847/0004-637X/830/2/79*

NASA/CXC & Weiss, M. (2008), '*Whirling Black Holes*'. [Accessed: 20.05.2021].
URL: *https://www.nasa.gov/mission_pages/chandra/multimedia/photos08-003.html*

Nulsen, P. E. J., McNamara, B. R., Wise, M. W. & David, L. P. (2005), 'The Cluster-Scale AGN Outburst in Hydra A', *The Astrophysical Journal* **628**(2), 629–636.
URL: *http://dx.doi.org/10.1086/430845*

Rosswog, S. & Bruggen, M. (2007), *Introduction to high-energy astrophysics*.

SAO (2019), '*Science Instruments*'. [Accessed: 13.05.2021].
URL: *https://chandra.si.edu/about/science_instruments.html*

SAO (2021), '*Chandra: About Chandra*'. [Accessed: 23.03.2021].
URL: *https://chandra.harvard.edu/about/*

Voit, G. M., Donahue, M., O'Shea, B. W., Bryan, G. L., Sun, M. & Werner, N. (2015), 'Supernova Sweeping and Black Hole Feedback in Elliptical Galaxies', *The Astrophysical Journal* **803**(2), L21.
URL: *http://dx.doi.org/10.1088/2041-8205/803/2/L21*

Werner, N. & Mernier, F. (2020), 'Hot Atmospheres of Galaxies, Groups, and Clusters of Galaxies', *Reviews in Frontiers of Modern Astrophysics* p. 279–310.
URL: *http://dx.doi.org/10.1007/978-3-030-38509-5_10*

Williams, F. (2018), *Combustion theory: the fundamental theory of chemically reacting flow systems*, 2 edn, CRC Press.

Zhang, C., Churazov, E., Forman, W. R. & Jones, C. (2018), 'Standoff distance of bow shocks in galaxy clusters as proxy for mach number', *Monthly Notices of the Royal Astronomical Society* **482**(1), 20–29.
URL: *http://dx.doi.org/10.1093/mnras/sty2501*